PAPER

Check for updates

Molecular insights into adhesive mechanisms of phosphate-based dental adhesives on zirconia surfaces: effects of zirconia crystal structure†

Yosuke Sumiya [ID] *[a] and Takahiro Uwabe[b]

This paper analyses the adhesion mechanisms of phosphate-based dental adhesives to zirconia materials based on density functional theory (DFT). Zirconia can be a mixture of three crystal structures: monoclinic, tetragonal and cubic. We investigated how these crystal surfaces influence adhesion. On all crystal surfaces, proton transfer occurs from the phosphate group in the adhesive to the zirconia surface. Among the surfaces, the monoclinic surface exhibits the highest adhesive strength. Interfacial interactions involving charge transfer are observed at all adhesive interfaces, which are particularly significant on the monoclinic surface. This is attributed to the low-coordination number of zirconium atoms specific to the monoclinic surface. Moreover, the strong Lewis basicity of these low-coordination zirconium atoms induces structural changes in the methacryloyl group, which acts as polymerization sites in the adhesive. These findings provide valuable insights for guiding the design of zirconia-based dental materials.

1. Introduction

Ceramics are increasingly used as metal-free dental restorative materials, especially zirconia (ZrO_2) due to its excellent mechanical properties and biocompatibility,[1,2] and are widely used in crown restorations and implant treatment. Zirconia takes monoclinic, tetragonal and cubic crystal structures depending on temperature,[3–5] with tetragonal and cubic being utilised as prosthetic materials due to their higher mechanical strength.[6,7] Zirconia is chemically stable and difficult to bond, and strategies to achieve strong adhesion are required. Conventional adhesion treatments for silica-based ceramic materials often involve the use of silane coupling agents such as 3-methacryloxypropyltrimethoxysilane (γ-MPS), which has been suggested to be ineffective for zirconia.[8–10]

In dental treatment using zirconia prosthetic materials, adhesives containing 10-methacryloyloxydecyl dihydrogen phosphate (10-MDP) as an adhesive monomer are commonly used.[11–13] 10-MDP is composed of methacryloyl groups, phosphate groups, and carbon chains linking them as shown in Fig. 1. The methacryloyl group acts as a polymerization group,

the phosphate group as an adhesive functional group, and the carbon chain as a spacer. These compounds are referred to as 10-MDP, 6-MHP, and 2-MEP depending on the length of the carbon chain (n = 5, 3, 1), respectively. 10-MDP has been experimentally suggested to form chemical bonds with zirconia surfaces.[14,15] However, the influence of pretreatments applied to zirconia surfaces should not be ignored. For example, sandblasting treatment increases the proportion of the monoclinic phase on the material, resulting in a mixture of the three crystal structures.[16,17] The zirconia surface activity depends on the crystal structure,[18–20] which may have a non-trivial effect on adhesion. The effect of this difference in crystal structure on adhesive strength and mechanisms is of interest, but direct observation of the adhesive layer remains a challenge as the layer is buried by the constituent materials.[21] Thus, the molecular-level effects of the different zirconia crystal structures on the interactions with 10-MDP need to be clarified theoretically.

Theoretical approaches using density functional theory (DFT) calculations and molecular dynamics (MD) simulations are available to elucidate the adhesion mechanism. For industrial adhesion, adhesive interactions for various materials have been analyzed in detail with these methods,[22–38] and the similar methods promise application to dental adhesive interfaces. In this study, we perform a systematic analysis based on DFT calculations to elucidate the effects of zirconia crystal structures on the adhesion mechanism. Specifically, we treat 2-MEP as an adhesive monomer instead of 10-MDP to efficiently

a Department of Applied Chemistry, Yamaguchi University, 2-16-1 Tokiwadai, Ube, Yamaguchi 755-8611, Japan. E-mail: yosuke.sumiya@yamaguchi-u.ac.jp

b Institute for Materials Chemistry and Engineering and IRCCS, Kyushu University, Nishi-Ku, Fukuoka 819-0395, Japan

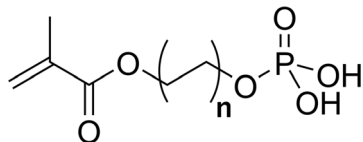† Electronic supplementary information (ESI) available. See DOI: https://doi.org/10.1039/d5tb00004a

This journal is © The Royal Society of Chemistry 2025

J. Mater. Chem. B, 2025, 13, 5095–5108 | 5095

Fig. 1 Chemical structure of the phosphate-based adhesive monomer. For n = 5, 3, and 1, these are called 10-MDP, 6-MHP, and 2-MEP, respectively.

analyze its interaction with each zirconia crystal surface and elucidate the adhesion mechanisms. The obtained findings are expected to contribute to the development of guidelines in adhesion to zirconia prosthetic materials.

2. Methodology

2.1 Modeling of ZrO2 surfaces

The crystal structures of monoclinic (m-ZrO$_2$),[39] tetragonal (t-ZrO$_2$),[40] and cubic (c-ZrO$_2$)[41] are optimized by DFT calculation. Each optimized structure is shown in Fig. 2. All DFT calculations are performed using the Vienna Ab initio Simulation Package (VASP) 5.4.4.[42–44] The Perdew–Burke–Ernzerhof (PBE) form of the generalized gradient approximation (GGA) is used as the exchange–correlation functional.[45] Dispersion interactions are accounted for using the Grimme D2 method.[46] The electron–ion interactions are treated with the projector augmented wave (PAW) method.[47,48] Computational parameters are set as follows: cutoff energy of the plane-wave basis set of 500 eV, k-point mesh spacing of $2\pi \times 0.05$ Å^{-1}, self-consistent field (SCF) convergence criterion of 1.0×10^{-5} eV, and atomic force threshold of 0.03 eV Å^{-1}.

In modelling of surface slab models for each crystal structure, the most stable surface is cut, incorporating a vacuum layer of approximately 23 Å. Each obtained structure is optimized to create the surface models **1a–3a** shown in Fig. 3. **1a**, **2a**, and **3a** correspond to (−111),[49,50] (101),[51,52] and (111)[53,54] surfaces, respectively. VESTA software[55] is used to visualize the structures. Additionally, to account for wet environment of oral cavity, we create surface models **1aw–3aw**, which are hydroxylated by the chemisorption of water molecules on the

surfaces. These are obtained by geometry optimization by coordinating OH groups on the top and bottom zirconium atoms and hydrogen atoms on the adjacent oxygen atoms for the clean surfaces **1a–3a**. Here, two hydrogen atoms from **1a** and one hydrogen atom from **2a** and **3a** transfer to the OH groups, resulting in the formation of water molecules.

2.2 Modeling of 2-MEP/ZrO2 surface complexes

To explore the stable conformation of 2-MEP on each zirconia surface, initial structures of 2-MEP randomly placed on ZrO$_2$ surfaces are generated and molecular dynamics (MD) simulations are performed in the Forcite module of Materials Studio software.[56] Here, the unit cells of the six surface models (**1a–3a** and **1aw–3aw**) are made into supercells to accommodate the 2-MEP molecule. The m-ZrO$_2$, t-ZrO$_2$, and c-ZrO$_2$ are extended to 2×2, 2×4, and 2×2, respectively. To explore the large conformational space of the 2-MEP, the MD simulations were performed in NVT ensemble with Nose–Hoover thermostat[57] at 500 K using the COMPASS force field.[58] The time step and evolution are 1.0 fs and 5.0 ns, respectively. All atoms in the zirconia surface are fixed and only the 2-MEP molecule are relaxed. Snapshots are obtained every 50 ps throughout the MD simulation, and 10 energetically stable structures are extracted from the 100 structures. DFT optimizations are then applied to the obtained 10 structures, where the first layer of zirconia surface and 2-MEP are relaxed, and others are fixed. The fixed atoms are visualized in Fig. S1 (ESI†). The most stable structures are adopted as complex models of 2-MEP and zirconia surfaces. Applying the above procedure to all zirconia surfaces **1a–3a** and **1aw–3aw** yields **1b–3b** and **1bw–3bw** shown in Fig. 4(a)–(f). The number of atoms in these structures are 160, 168, 168, 256, 264, and 264, respectively.

The adhesive interface models obtained in this manner is the most minimal and allows for efficient analysis of the interactions between the zirconia surfaces and the adhesive. The effects of metastable conformations and interactions between adhesive molecules are excluded from these models. Furthermore, considering a more realistic environment such as oral cavity, the effects of physisorbed waters accumulated on the zirconia surface, stains in oral cavity, changes in surface
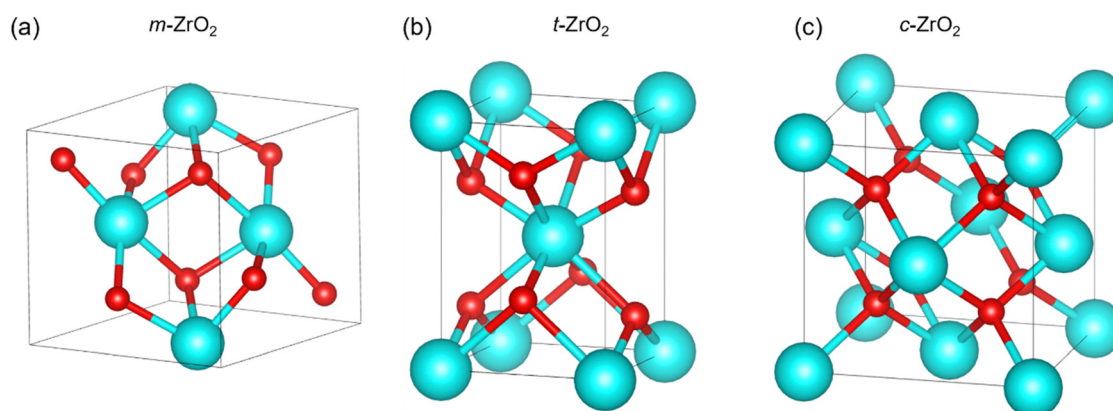

Fig. 2 Crystal structures of zirconia. (a) m-ZrO$_2$, (b) t-ZrO$_2$, (c) c-ZrO$_2$.

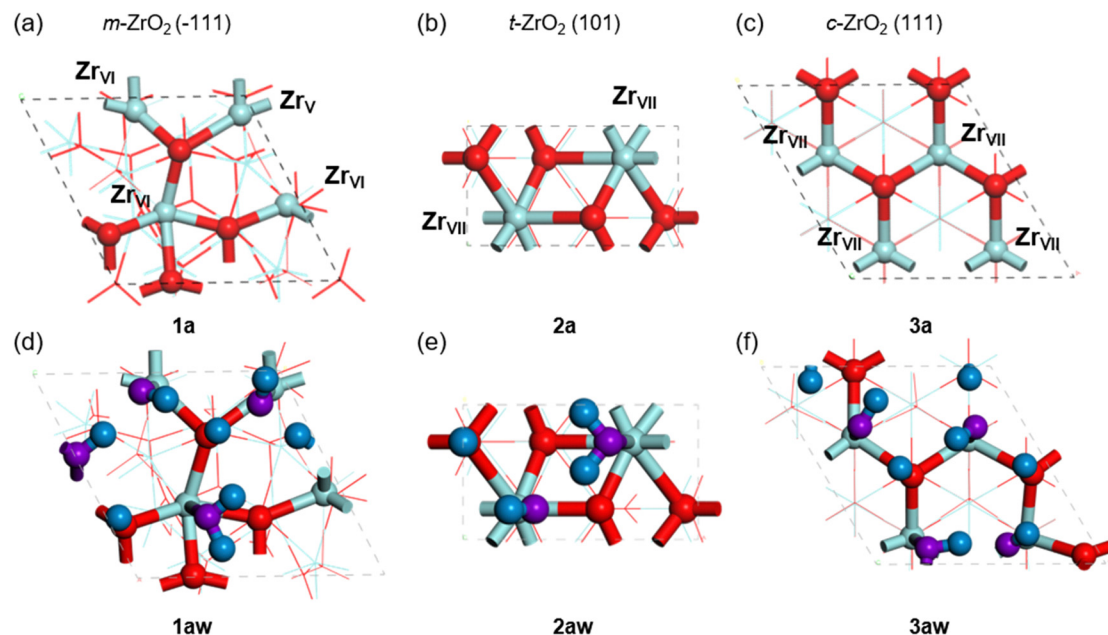5096 | J. Mater. Chem. B, 2025, **13**, 5095–5108

This journal is © The Royal Society of Chemistry 2025

Fig. 3 Top views of zirconia surfaces. (a) m-ZrO_2 (−111), (b) t-ZrO_2 (101), (c) c-ZrO_2 (111) surfaces. (d)−(f) are hydroxylated surfaces of (a)−(c). Zirconium and oxygen atoms in zirconia are represented by light blue and red, respectively, and hydrogen and oxygen atoms in adsorbed water are represented by dark blue and purple, respectively.
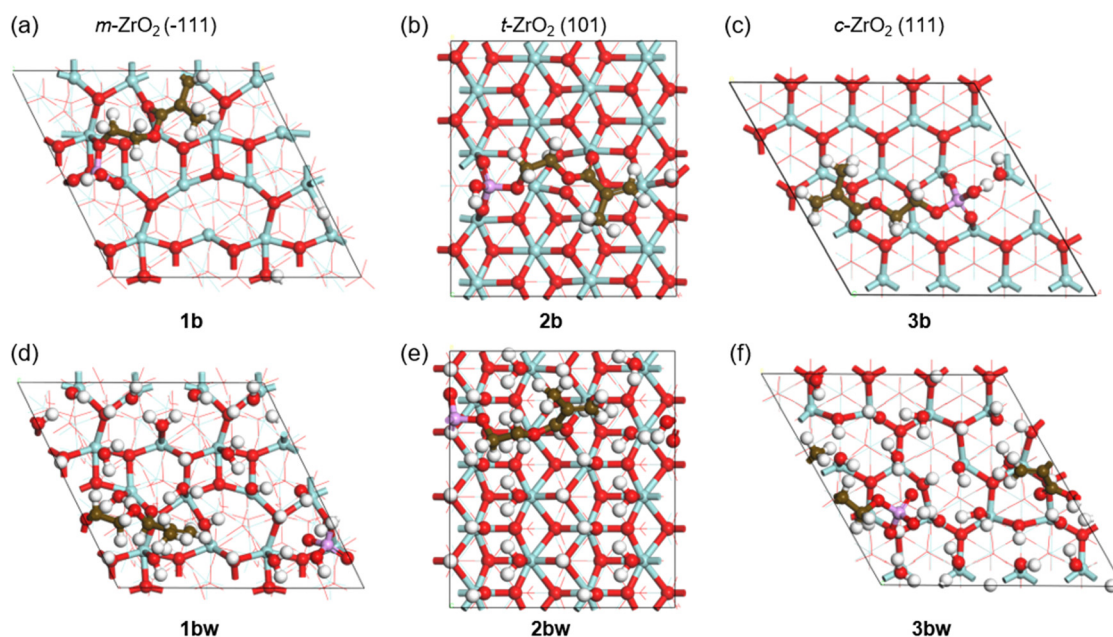

Fig. 4 Top views of the most stable structures of the 2-MEP molecule. (a) m-ZrO_2 (−111), (b) t-ZrO_2 (101), (c) c-ZrO_2 (111) surfaces. (d)−(f) are hydroxylated surfaces of (a)−(c). The chemical bonds in low layers are drawn with fine lines.

condition due to pretreatment with hydrofluoric acid, and trace amounts of yttrium atoms in the zirconia may not be negligible. These task remains open for future work.

2.3 Calculation of adhesive strength

The tensile adhesive strength is estimated by differentiating the potential energy curve of the 2-MEP molecule dissociating perpendicularly from the surface with respect to the displacement. To obtain the potential energy curves for the six 2-MEP/ZrO_2 interfaces obtained by the above procedure, the 2-MEP molecule is dissociated from the surface to 8.0 Å in 0.1 Å increments, yielding 80 structures. Here, for systems in which proton transfer from the phosphate groups in the 2-MEP to the surface occurs, the portion of the 2-MEP excluding

This journal is © The Royal Society of Chemistry 2025

J. Mater. Chem. B, 2025, **13**, 5095–5108 | **5097**

the proton is vertically displaced. Single-point calculations are performed for each structure, plotted in terms of energy E with respect to the displacement Δr of the center of gravity of the 2-MEP molecule and fitted to the Morse potential:

$$E = D(1 - e^{-a\Delta r})^2 \qquad (1)$$

where D represents the adhesive energy and a is a constant specific to the system. The most stable position on the surface is set to $\Delta r = 0$. Differentiating the obtained fitting curve with respect to Δr yields the adhesive force F expressed by the following equation:

$$F = \frac{dE}{d\Delta r} \qquad (2)$$

The maximum value on the adhesive force–displacement (F–Δr) plot is estimated as the adhesive strength F_{ad}.

$$F_{ad} = \max(F) \qquad (3)$$

The energy E can be de composed into two parts: the dispersion contribution and the other DFT contribution. That is, E is expressed as a simple sum of the energies of the dispersion and DFT contributions ($E_{dispersion}$ and E_{DFT}):

$$E = E_{dispersion} + E_{DFT} \qquad (4)$$

Differentiating both sides of the above equation leads to the following relationship for the adhesive force F, which can also be decomposed into dispersion and DFT forces ($F_{dispersion}$ and F_{DFT}):

$$F = F_{dispersion} + F_{DFT} \qquad (5)$$

The E_{DFT} is fitted to the equation that translates the Morse potential in the z direction by α, expressed as:

$$E_{DFT} = D_{DFT}(1 - e^{-a_{DFT}\Delta r})^2 + \alpha \qquad (6)$$

Differentiating the obtained fitting curve with respect to displacement yielded the F_{DFT}, and subtracting it from F yielded the $F_{dispersion}$. This decomposition analysis is used to evaluate the contribution of each component.

2.4 Visualization of interfacial interactions based on charge density difference analysis

Charge density difference is available for analyzing interactions involving charge transfer at adhesive interfaces.[59] The difference of the charge density before and after adhesion allows for visualizing the interactions between the 2-MEP and the surface when 2-MEP is adsorbed on the surface. The difference of charge density is expressed by the following equation:

$$\Delta\rho_{ad} = \rho_{complex} - (\rho_{surface} + \rho_{adhesive}) \qquad (7)$$
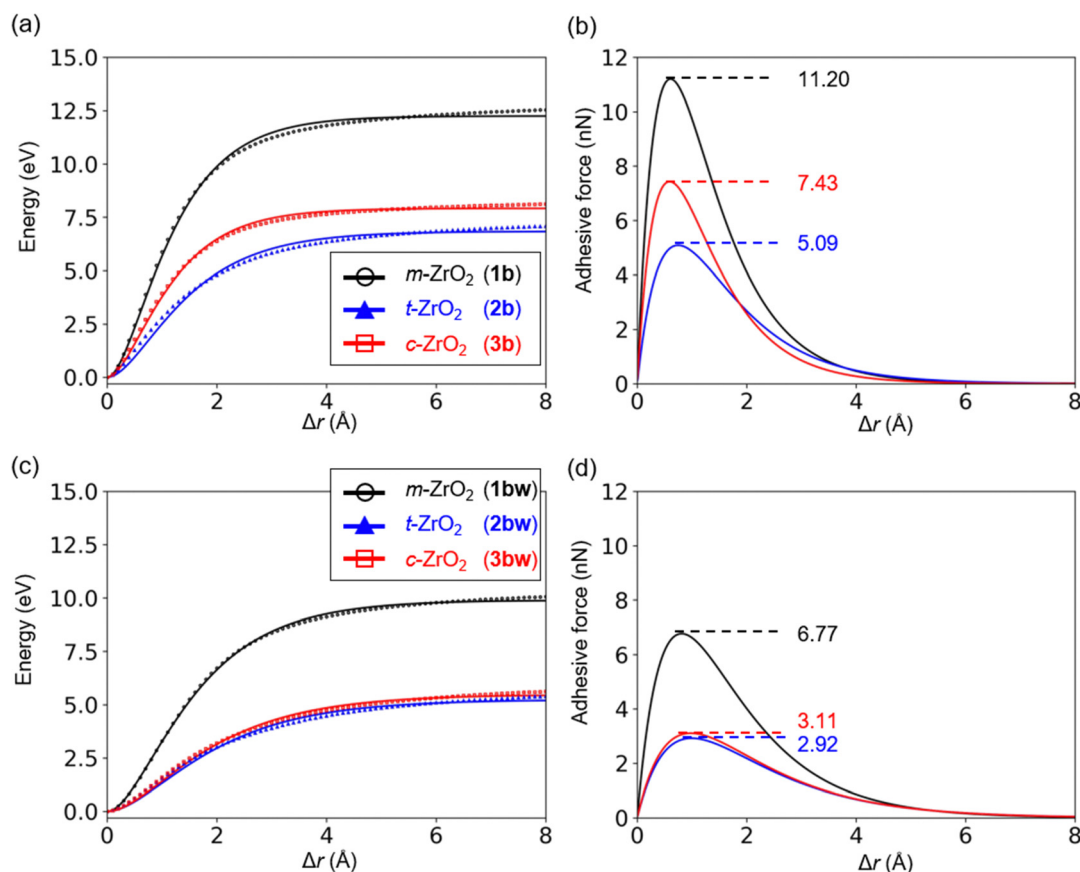

Fig. 5 (a) Energy and (b) adhesive force curves of the clean surface of zirconia. Black, blue, and red lines correspond to m-ZrO$_2$ (−111), t-ZrO$_2$ (101), c-ZrO$_2$ (111) surfaces (**1b–3b**). (c) and (d) are the energy and adhesive force curves for the hydroxylated surfaces (**1bw−3bw**).

5098 | *J. Mater. Chem. B*, 2025, **13**, 5095–5108

This journal is © The Royal Society of Chemistry 2025

where $\rho_{complex}$ is the charge density of the complex consisting of the surface and 2-MEP molecule, and $\rho_{surface}$ and $\rho_{adhesive}$ are the charge density of the surface and 2-MEP molecule, respectively. These are computed separately and their atomic coordinates are fixed as the same as those in the complex.

For interaction sites visualized by the charge density difference analysis, their binding energies can be estimated by calculating their crystal orbital Hamilton population (COHP).[60] The binding energy is useful in identifying the atom pairs that contribute to stability in the adsorbed structure. The COHP analysis allows the affinity of each functional group and its interaction-site in the adhesive to the surface to be evaluated. The COHP analysis requires the plane wave function to be projected to a localized basis set. The local orbital basis suit towards electronic-structure reconstruction (LOBSTER) software[61] was used for this procedure. Using the Hamiltonian matrix element and crystal orbital expansion coefficients, the density of states (DOS) of a given atomic pair is decomposed into bonding and antibonding energy regions to obtain the projected COHP (pCOHP).[62] The bonding interaction is a negative value due to negative Hamiltonian matrix elements involved. Integrating the pCOHP up to the Fermi level E_F provides the binding energy of the corresponding
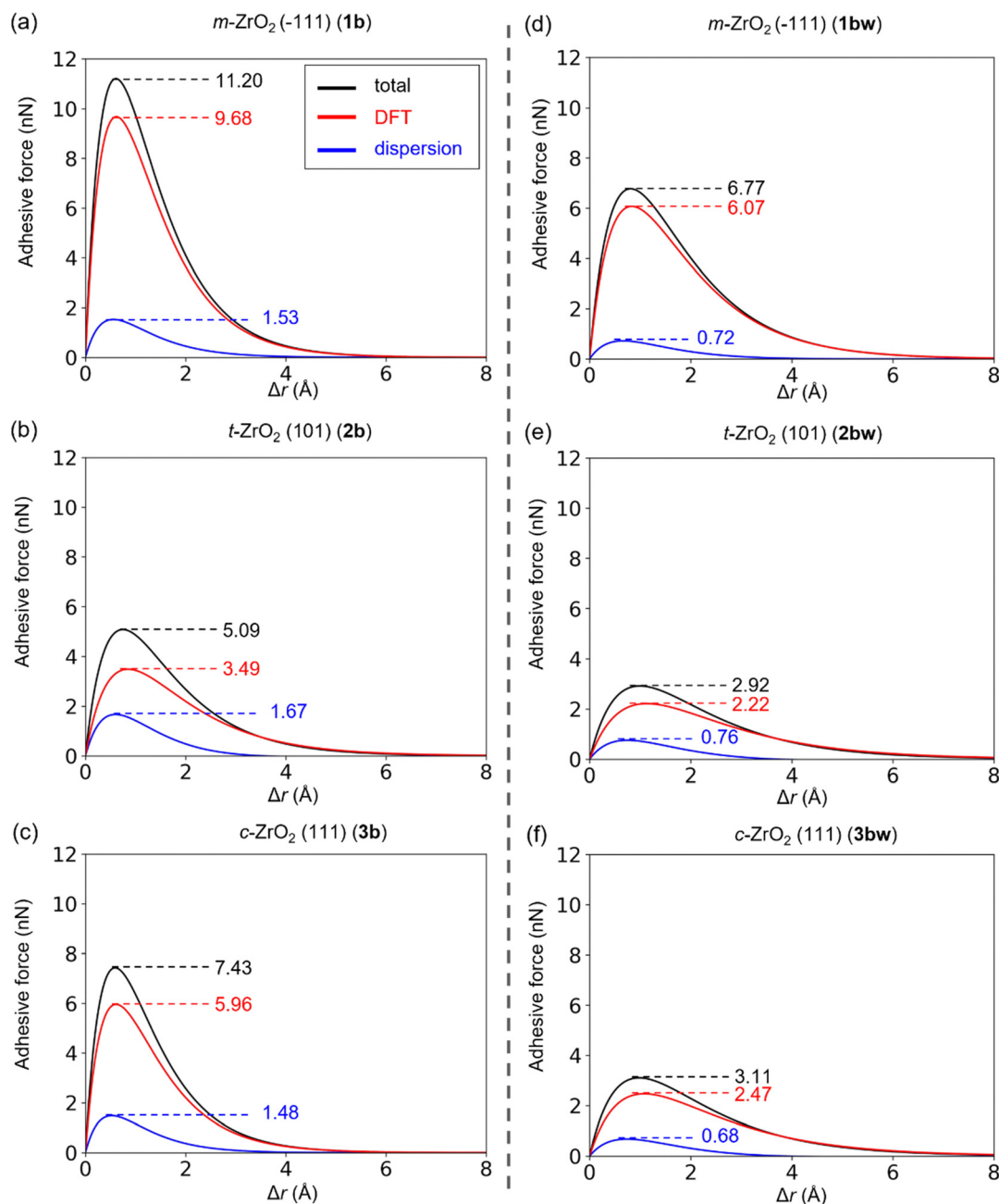

Fig. 6 Decomposition of the adhesive force curves into dispersion and DFT components, where **1b–3b** correspond to (a)–(c), **1bw–3bw** correspond to (d)–(f), respectively. Black, blue, and red represent the overall, dispersion, and DFT adhesive force curves, respectively.

This journal is © The Royal Society of Chemistry 2025

J. Mater. Chem. B, 2025, 13, 5095–5108 | 5099

atomic pair. This value is the integrated crystal orbital Hamilton population (ICOHP) and is expressed as the following equation:[63]

$$ICOHP = \int_{-\infty}^{E_F} pCOHP\ (E)\ dE \qquad (8)$$

A negative ICOHP value means that the atomic pair has a strong bonding interaction, and the strength of the interaction can be compared using ICOHP values. Here, we emphasize the difference between DFT calculations and classical force-field calculations in that DFT calculations allow precise analysis of interactions involving charge transfer and chemical reactions (bond-rearrangement), whereas such interactions and reactions are difficult to simulate with force-field calculations.

3. Results and discussion

3.1 Energy and adhesive force curves of 2-MEP for zirconia surfaces

Fig. 5(a) shows the dissociation energy curves of the 2-MEP molecule for **1b**–**3b** shown in Fig. 4. These energy curves have a single inflection point. The black, blue and red colors correspond to the **1b**, **2b** and **3b** energy curves respectively, where the points on the curves are the computed values and the solid lines are the fitting curves of the Morse potential expressed in eqn (1). The Morse potential parameters D, the depth of the potential well, are 12.3, 6.8, and 7.9 eV, respectively. Fig. 5(b) shows the adhesive force curves obtained by differentiating the energy curves. The adhesive strengths, F_{ad}, of **1b**–**3b** are 11.20, 5.09, and 7.43 nN, respectively. The order of D and F_{ad} magnitude corresponds, **1b** > **3b** > **2b**.

Fig. 5(c) and (d) show the energy and adhesive force curves for the hydroxylated surfaces (**1bw**–**3bw**). The D values are 9.9, 5.2 and 5.5 eV, respectively, with decreasing values on all surfaces, indicating that all potential wells are shallower by surface hydroxylation. The F_{ad} values are 6.77, 2.92 and 3.11 eV, respectively. Surface hydroxylation results in adhesive strengths of 61, 57 and 42% for the m-ZrO$_2$ (−111), t-ZrO$_2$ (101) and c-ZrO$_2$ (111) surfaces, respectively. In other words, surface hydroxylation reduces the adhesive strength by approximately half. F_{ad} at the monoclinic (**1b** and **1bw**) is larger than at the other interfaces. Although direct comparison with experimental values remains difficult, this result is qualitatively consistent with the fact that sandblasting increases the monoclinic surface and improves the adhesive strength.[16] What is the reason for the difference in adhesive strength for each crystal surface? To identify the reason, the energy is decomposed into dispersion and DFT contributions using eqn (4) and (5).

Fig. 6(a)–(c) shows the decomposition of the **1b**–**3b** adhesive force curves into F_{DFT} and $F_{dispersion}$ curves, respectively, where black, blue, and red colors represent the F, $F_{dispersion}$, and F_{DFT} curves. As can be seen in the figure, F_{DFT} is larger than $F_{dispersion}$ for all **1b**–**3b**. This means that the DFT contribution is dominant at the 2-MEP/clean ZrO$_2$ interface. The maximum of the dispersion-contributed adhesive strength, $F_{dispersion}^{max}$, is **2b** > **1b** > **3b** (1.67 nN > 1.53 nN > 1.48 nN), while the maximum of

the DFT-contributed adhesive strength, F_{DFT}^{max}, is **1b** > **3b** > **2b** (9.68 nN > 5.96 nN > 3.49 nN), corresponding to the order of the overall adhesive strength, F_{ad}.

Fig. 6(d)–(f) shows the decomposition of the **1bw**–**3bw** adhesive force curves into F_{DFT} and $F_{dispersion}$ curves. As with clean surfaces **1b**–**3b**, F_{DFT} is larger than $F_{dispersion}$ for **1bw**–**3bw**. It is thus suggested that the DFT contribution is dominant in
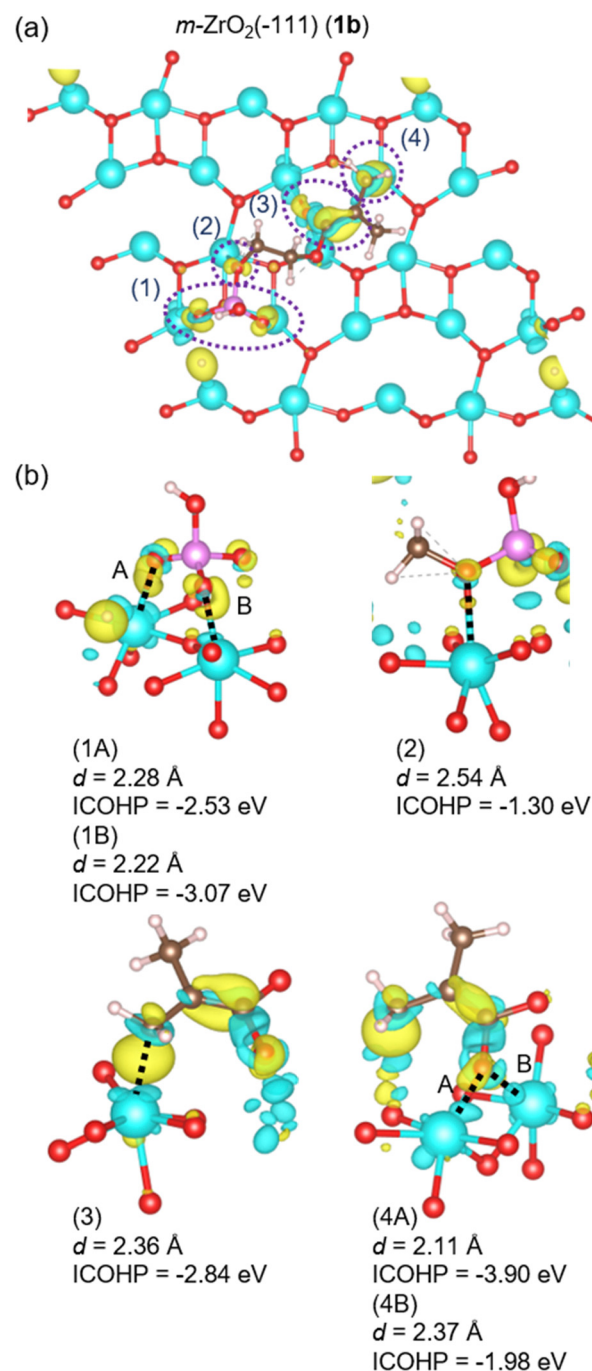

Fig. 7 Charge density differences of **1b** (m-ZrO$_2$). (b) Enlarged views of sites (1)–(4) from different angles. Interatomic distances d and ICOHP values for the corresponding atomic pairs are shown. Interactions (1) and (4) are labelled as (1A) and (1B), and (4A) and (4B), respectively, as they involve two atomic pairs.

5100 | *J. Mater. Chem. B*, 2025, **13**, 5095–5108

This journal is © The Royal Society of Chemistry 2025

adhesive strength, regardless of surface hydroxylation. As can be seen in the figure, $F_{\text{dispersion}}^{\max}$ order **2bw** > **1bw** > **3bw** (0.76 nN > 0.72 nN > 0.68 nN) is inconsistent with F_{ad} order, while $F_{\text{DFT}}^{\max}$ order **1bw** > **3bw** > **2bw** (6.07 nN > 2.47 nN > 2.22 nN) is consistent with F_{ad} order. Furthermore, the differences of $F_{\text{DFT}}^{\max}$ of **2bw** and **3bw** with respect to **1bw** (3.85 nN and 3.60 nN) are larger than those of $F_{\text{dispersion}}^{\max}$. Accordingly, the difference in F_{ad} on the hydroxylated surfaces is also suggested to depend on the difference in DFT contribution. The interfacial interactions originating from the DFT contribution involve charge transfer. In the next section, the interfacial interactions with charge transfer are visualized using charge density difference analysis and the factors contributing to the high adhesive strength to the m-ZrO$_2$ surfaces (**1b** and **1bw**) are discussed.

3.2 Interfacial interactions for 2-MEP/ZrO$_2$ interfaces

To clarify the effects of changes in molecular structure and charge density that contribute to differences in the adhesion of 2-MEP, the charge density difference analysis is applied to all of the interfaces (**1b**–**3b** and **1bw**–**3bw**) based on eqn (7). Fig. 7 and 8 show the difference of charge density for **1b** and that for **2b** and **3b**, respectively. Yellow and cyan colors represent the charge accumulation and depletion. For visibility, only the surface layer is shown. The isosurface value was set to 0.01 e Å^{-3}.

Fig. 7(a) shows the sites where significant charge density changes are observed in **1b**, marked by the purple dotted lines (1)–(4). These enlarged views from different angles are represented in Fig. 7(b), with the distances d of the interacting
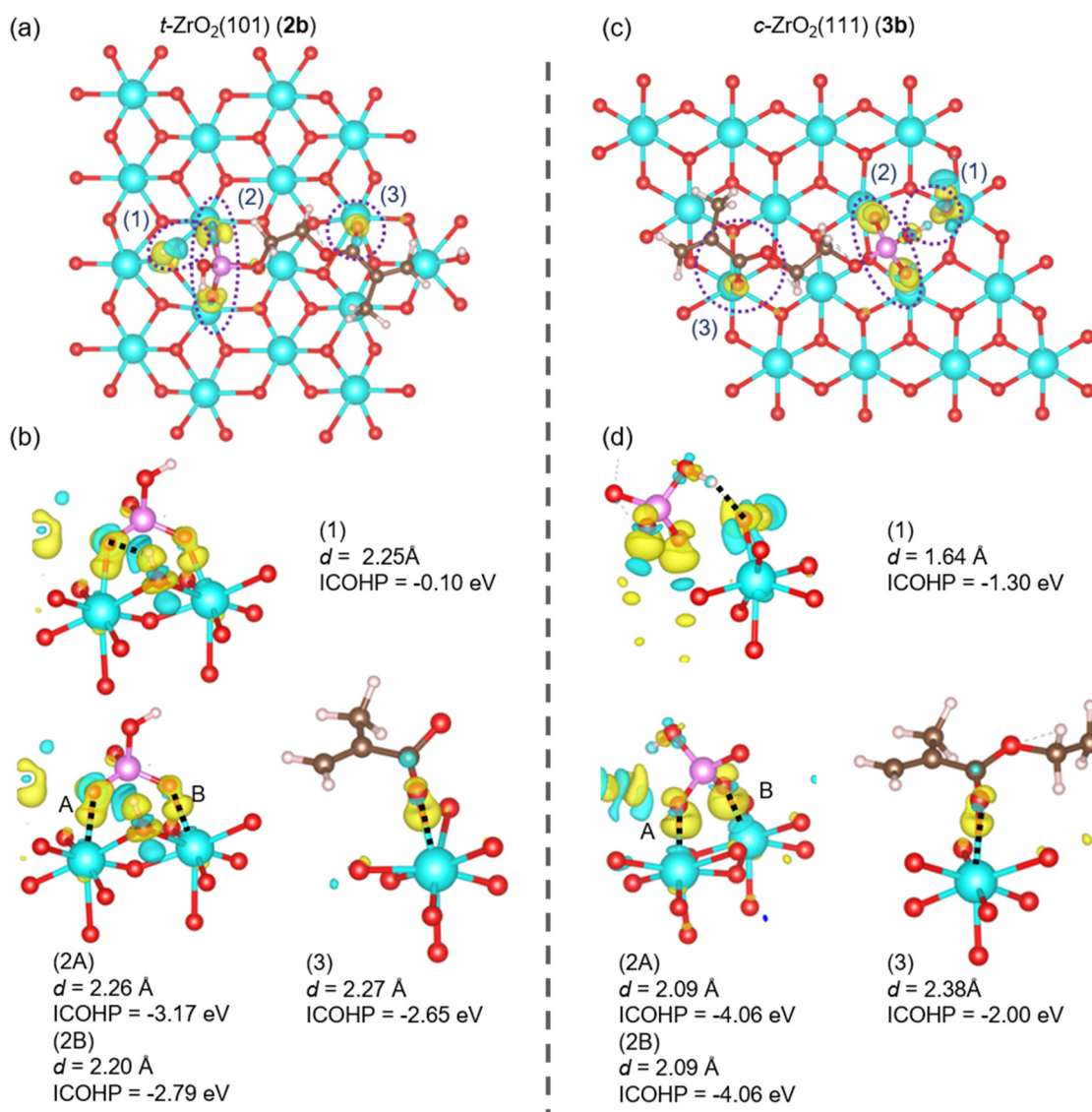

Fig. 8 (a) and (c) Charge density differences of **2b** (t-ZrO$_2$) and **3b** (c-ZrO$_2$). (b) and (d) Enlarged views of sites (1)–(3) in (a) and (c) from different angles. Interatomic distances d and ICOHP values for the corresponding atomic pairs are shown. Interactions (2) in **2b** and **3b** are labelled as (2A) and (2B), as they involve two atomic pairs.

This journal is © The Royal Society of Chemistry 2025

J. Mater. Chem. B, 2025, **13**, 5095–5108 | **5101**

atomic pairs and their ICOHP values. In **1b**, proton transfer from the phosphate group of the 2-MEP to the surface occurs. After the proton transfer, the two oxygen atoms of the phosphate group strongly interact with the surface zirconium atoms, as labelled in (1A) and (1B), with their ICOHP values of −2.53 and −3.07 eV, respectively. The ICOHP value of the interaction between the oxygen atom of the 2-MEP labelled by (2) and the surface zirconium atom is −1.30 eV. Additionally, the ICOHP values for (3), where the carbon atom of the methacryloyl group interacts with the zirconium atom on the surface, and (4A) and (4B), where the oxygen atom of the methacryloyl group interacts with the two zirconium atoms on the surface, are −2.84, −3.90, and −1.98 eV, respectively.

Fig. 8(a) and (c) show the sites of significant charge density changes in **2b** and **3b**, marked by the purple dotted lines (1)–(3). These enlarged views from different angles are represented in (b) and (d). Proton transfer from the phosphate group of the 2-MEP to surface oxygen atoms also occurs in **2b** and **3b**. In **2b**, the proton transferred to the surface changes to OH group, which interacts with the oxygen atom of the phosphate group. This is labelled (1) and its ICOHP value is −0.10 eV. Furthermore, the two oxygen atoms of the phosphate group interacted with the zirconium atoms on the surface. These labels are (2A) and (2B) and their ICOHP values are −3.17 and −2.79 eV respectively. In addition, the ICOHP value of the site (3) where the oxygen atom of the methacryloyl group interacts with the zirconia atom on the surface is −2.65 eV. In **3b**, the proton transferred to the oxygen atom on the surface also changes to OH group. The interaction between the oxygen atom of the OH group and the hydrogen atom of the phosphate group in 2-MEP is labelled (1), with the ICOHP value of −1.30 eV. The oxygen atoms that released the proton of the phosphate group and double-bonded to phosphorus atom interact with the zirconium atoms on the surface. These interaction sites are labelled (2A) and (2B) with their ICOHP values of both −4.06 eV. Furthermore, the oxygen atom of the methacryloyl group interacts with the zirconium atom on the surface. This is labelled (3) with its ICOHP value of −2.00 eV.

Table 1 shows the ICOHP values of the interfacial interactions in **1b–3b**, classified by those derived from the phosphate and methacryloyl group, respectively. The absolute value of the sum of ICOHPs for the phosphate group-derived interactions with the surface |ICOHP| shows the highest value at **3b**, while the methacryloyl group-derived |ICOHP| showed
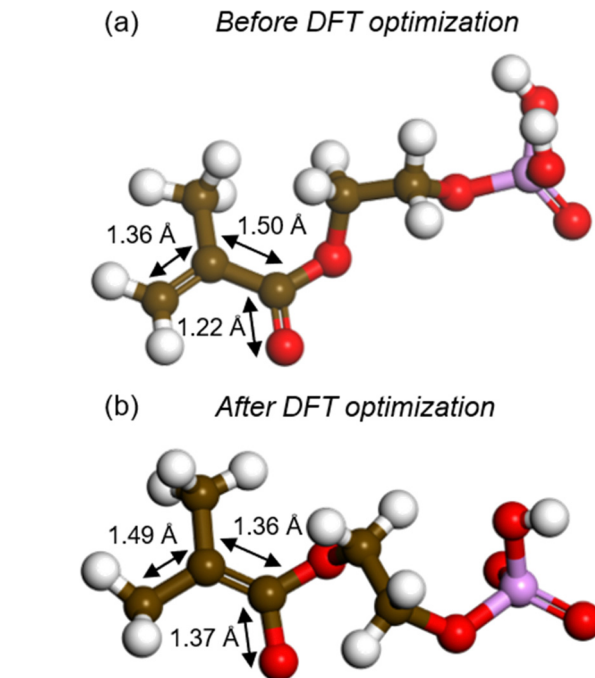

Fig. 9 Structural change of 2-MEP in **1b** by DFT optimization. (a) and (b) represent the structures before and after the DFT optimization, respectively.

the highest value at **1b**. The total ICOHP values for **1b–3b** are −15.63, −8.70 and −11.42 eV, respectively. The order of these absolute values is **1b** > **3b** > **2b**, which is the same as the order of adhesive strength. The results suggest that the interactions involving charge transfer contribute significantly to the difference in adhesive strength to each surface. The |ICOHP| of the methacryloyl group-derived interactions in **1b** is 8.73 eV, which is 6.08 and 6.73 eV larger than **2b** (2.65 eV) and **3b** (2.00 eV), respectively. In contrast, the |ICOHP| of the phosphate group-derived interactions in **1b** is 6.90 eV, which is 0.85 eV larger than **2b** (6.05 eV) and 2.52 eV less than **3b** (9.42 eV). In comparison with **1b**, the difference in |ICOHP| of the methacryloyl group-derived interactions is larger than that of the phosphate group-derived ones, suggesting that the larger adhesive strength of **1b** is due to the methacryloyl group-derived interactions.

Focusing on the interactions of the methacryloyl groups in **1b–3b**, only in **1b**, the carbon atom of the methacryloyl group

Table 1 ICOHP values for interactions derived from phosphate and methacryloyl groups in **1b–3b** and their sums. Parentheses indicate the label number of the interaction with its ICOHP value

	ICOHP (eV)	
	Phosphate group	Methacryloyl group
1b	(1A) −2.53, (1B) −3.07, (2) 1.30	(3) −2.84, (4A) −3.90, (4B) −1.98
1b-total	−6.90	−8.73
2b	(1) −0.10, (2A) −3.17, (2B) −2.79	(3) −2.65
2b-total	−6.05	−2.65
3b	(1) −1.30, (2A) −4.06, (2B) −4.06	(3) −2.00
3b-total	−9.42	−2.00

5102 | *J. Mater. Chem. B*, 2025, **13**, 5095–5108

This journal is © The Royal Society of Chemistry 2025

interacts with the zirconium atom on the surface (interaction (3)). Then, the sp^2 carbon atom changes to sp^3-like. In addition, the methacryloyl group in 2-MEP adsorbs on the **1a** (m-ZrO$_2$) surface, increasing the interatomic distance of the C=O double bond, while shortening the C–C single bond and resulting in double bond-like. Fig. 9 shows the structural changes of **1b** before and after the DFT optimization. This structural change can originate from the low-coordination number of zirconium atoms on the **1a** surface. On the **1a** surface are 5- and 6-coordinated zirconium atoms (Zr$_V$ and Zr$_{VI}$), which are absent in **2a** and **3a** shown in Fig. 3, and these are highly Lewis basic. These electron-rich zirconium atoms form chemically bonded Zr–C and Zr–O interactions by the charge transfer described by (3) and (4) in **1b**, shown in Fig. 7. These results suggest that the coordination number, *i.e.*, electronic state, of zirconium atoms on the surface has a significant effect on the adhesion to zirconia surface and can also induce structural changes in

2-MEP. Here, it should be emphasized that these results are obtained by adopting analysis based on DFT calculations. Proton transfer, structural changes of methacryloyl group, and charge transfer interactions are difficult to analyze using force field calculations. These molecular insights are critical novelties of this study.

Charge density difference analysis is also applied to **1bw**–**3bw** in the same manner as for **1b**–**3b**. Fig. 10 and 11 show the differences of charge density for **1bw** and those for **2bw** and **3bw**, respectively. In Fig. 10(a), the sites of significant charge density changes at **1bw** are indicated by purple dotted lines (1) and (2). These enlarged views from different angles are represented in (b). In **1bw**, proton transfer also occurs from the phosphate group in the 2-MEP, and this proton is transferred to the carbon atom of the methacryloyl group in the 2-MEP, where the proton is highlighted by purple dotted line. The structures before and after this proton transfer are shown in (c) and (d).
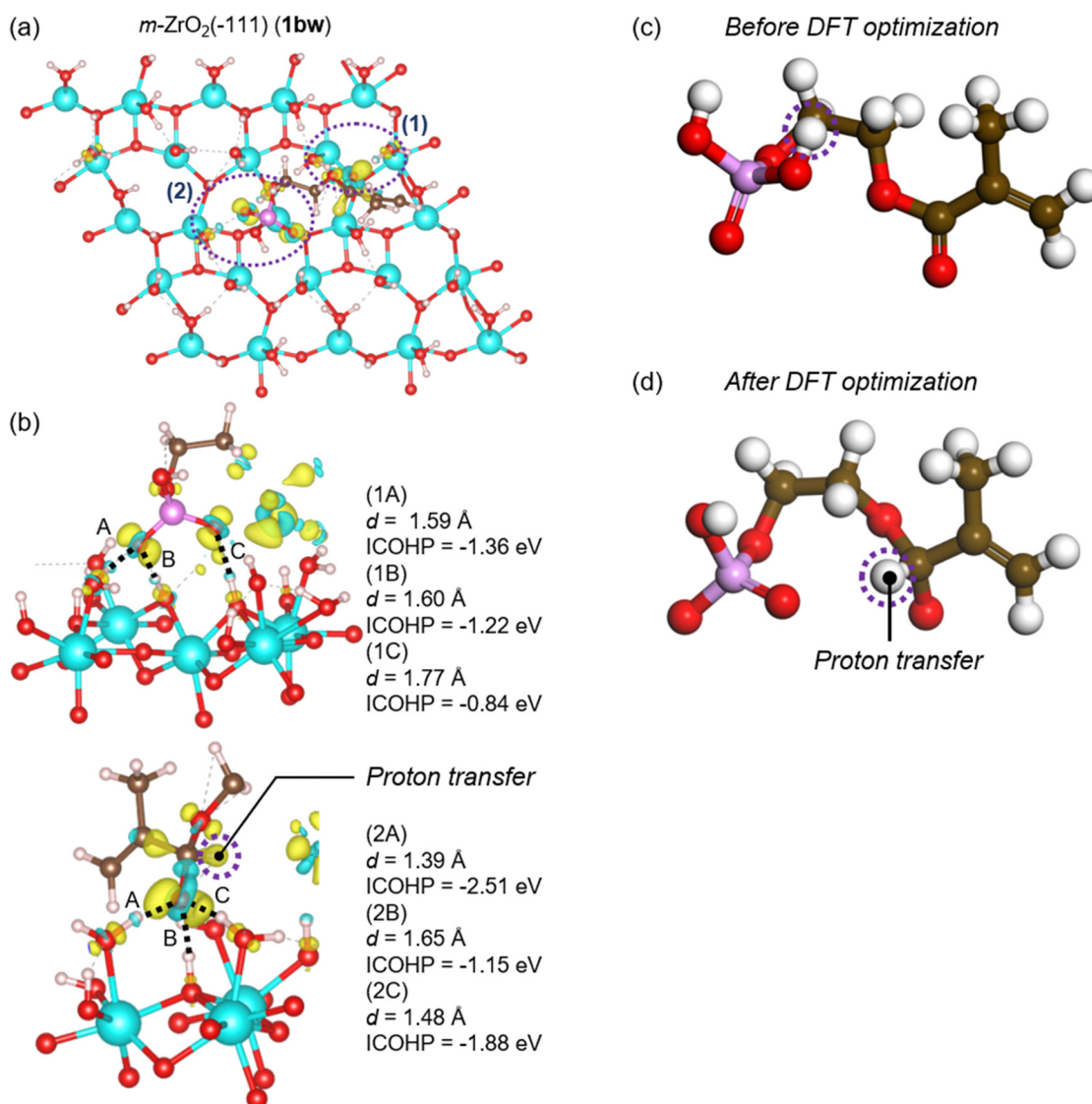

Fig. 10 (a) Charge density differences of **1bw**. (b) Enlarged views of sites (1) and (2) from different angles. (c) and (d) represent the 2-MEP structures in **1bw** before and after the DFT optimization, respectively.

This journal is © The Royal Society of Chemistry 2025

J. Mater. Chem. B, 2025, **13**, 5095–5108 | **5103**

After the proton transfer, the two oxygen atoms of the phosphate group interact with the hydroxy group on the surface by hydrogen bonding, as labeled in (1A)–(1C). Their ICOHP values are −1.36, −1.22, and −0.84 eV, respectively. The interactions of the methacryloyl groups in 2-MEP with the surface are labeled (2A), (2B), and (2C), and their ICOHP values are −2.51, −1.15, and −1.88 eV, respectively. These strong interactions attributed to the methacryloyl group are due to the proton

transfer that changes the C=O double bond to a single bond-like structure, resulting in an electron deficiency in the oxygen atom.

Fig. 11(a) and (c) show the sites of significant charge density changes in **2bw** and **3bw**, which are indicated by purple dotted lines (1), (2), and (3), respectively. These enlarged views from different angles are represented in (b) and (d). In both **2bw** and **3bw**, proton transfer occurs from the phosphate group of the
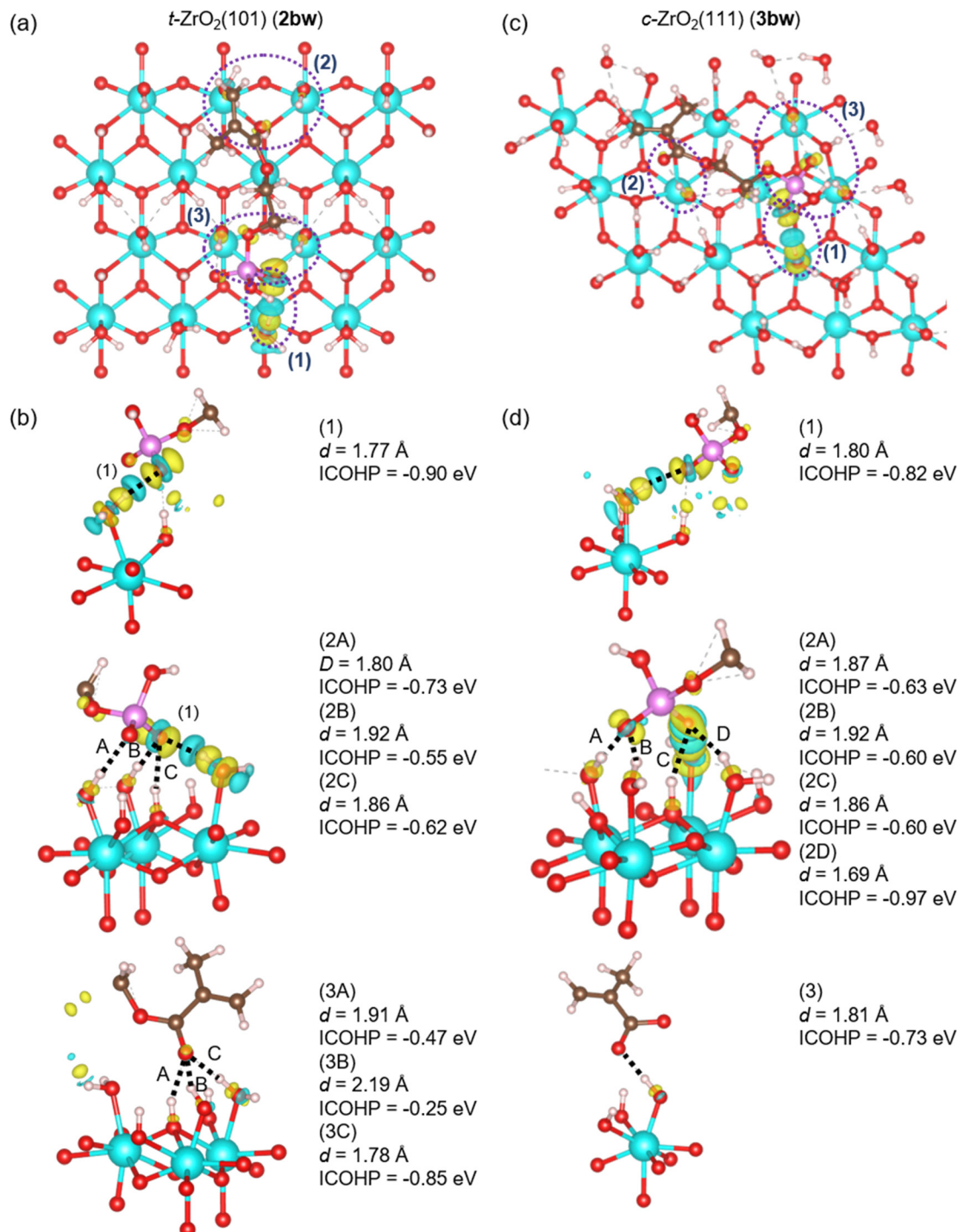

Fig. 11 (a) and (c) Charge density differences of **2bw** and **3bw**. (b) and (d) Enlarged views of sites (1)–(3) in (a) and (c) from different angles.

5104 | *J. Mater. Chem. B*, 2025, **13**, 5095–5108

This journal is © The Royal Society of Chemistry 2025

Table 2 ICOHP values for interactions derived from phosphate and methacryloyl groups in **1bw–3bw** and their sums. Parentheses indicate the label number of the interaction with its ICOHP value

	ICOHP (eV)	
	Phosphate group	Methacryloyl group
1bw	(1A) −1.36, (1B) −1.22, (1C) −0.84	(2A) −2.51, (2B) −1.15, (2C) −1.88
1bw-total	−3.42	−5.54
2bw	(1) −0.90, (2A) −0.73, (2B) −0.55, (2C) −0.62	(3A) −0.47, (3B) −0.25, (3C) −0.85
2bw-total	−2.80	−1.57
3bw	(1) −0.82, (2A) −0.63, (2B) −0.60, (2C) −0.60, (2D) −0.97	(3) −0.73
3bw-total	−3.62	−0.73

2-MEP to the hydroxy group on the surface. As for the interface interactions in **2bw**, (1) is the interaction between the transferred proton on the surface and the oxygen atom in 2-MEP, with the ICOHP value of −0.90 eV. Additionally, the oxygen atom of the P=O double bond in the phosphate group and the oxygen atom after releasing the proton form interactions with the hydroxy groups on the surface, which are labeled (2A), (2B), and (2C), respectively. These ICOHP values are −0.73, −0.55, and −0.62 eV. The oxygen atom of the methacryloyl group interacts with the hydroxy groups on the surface, which are (3A)–(3C). These ICOHP values are −0.47, −0.25, and −0.85 eV. The interface interactions in **3bw** are similar to those in **2bw**, and (1) is the interaction between the transferred proton on the surface and the oxygen atom in the 2-MEP, with the ICOHP value of −0.82 eV. The oxygen atom after releasing the proton of the phosphate group and the oxygen atom of the P=O double bond form the interactions with the hydroxy groups on the surface, which are labeled (2A), (2B), (2C), and (2D), respectively. These ICOHP values are −0.63, −0.60, −0.60, and −0.97 eV. The oxygen atom of the methacryloyl group forms the interaction (3) with the hydroxy group on the surface, with the ICOHP value of −0.73 eV.

Table 2 shows the classification of the **1bw–3bw** interfacial interactions and their ICOHP values according to the phosphate and methacryloyl group origin, respectively. The absolute value of the sum of the ICOHPs for the phosphate group-derived interactions |ICOHP| is largest at **3bw**, while the value of the methacryloyl group-derived |ICOHP| is largest at **1bw**. This tendency is the same as that of the clean surface systems **1b–3b**. The total ICOHP values for **1bw–3bw** are −8.96, −4.37, and −4.35 eV, respectively, and the order of these absolute values is **1b > 2b ≈ 3b**. These results suggest that charge transfer interactions contribute significantly to the difference in adhesive strength even on the hydroxylated surfaces. The |ICOHP| of the methacryloyl group-derived interactions in **1bw** is 5.54 eV, which is 3.97 and 4.81 eV larger than in **2bw** (1.57 eV) and **3bw** (0.73 eV), respectively. In contrast, the |ICOHP| of the phosphate group-derived interactions in **1bw** is 3.42 eV, which is larger than in **2bw** (2.80 eV) and slightly smaller than in **3bw** (3.62 eV). In comparison with **1bw**, the difference in methacryloyl group-derived interactions |ICOHP| is larger than that of phosphate group-derived ones, suggesting that the larger adhesive strength of **1bw** is due to methacryloyl group-derived interactions.

On the monoclinic surface, structural changes of the methacryloyl group are observed even in metastable structures other than the most stable (**1bw**). Fig. 12(a) shows **1bw**, and (b) and (c) show the metastable structures (**1cw** and **1dw**), where green represents the hydrogen atoms originally contained in the 2-MEP and white represents the hydrogen atoms originally on the surface. Each transferred hydrogen atom is highlighted by purple dotted lines. As can be seen in the figure, the hydrogen atoms in the phosphate group and on the surface move to the methacryloyl group. They are energetically close, and **1cw** and **1dw** are more unstable than **1bw** by only 0.04 eV (4.1 kJ mol^{-1}) and 0.07 eV (6.7 kJ mol^{-1}), respectively. That is, all structures can exist thermodynamically. Note that these structures are obtained from simple DFT optimization calculations. In other words, the reactions that lead to these structures can easily proceed with no barrier when 2-MEP approaches the monoclinic surface. Accordingly, various conformations of the 2-MEP other than the most stable structure may also induce structural changes in the methacryloyl group.

Finally, the adhesive strength of 2-MEP is largest on both clean and hydroxylated zirconia surfaces in the case of monoclinic crystals. The low-coordination number zirconium atoms on the monoclinic surface are highly Lewis basic, which induces proton transfer of 2-MEP and structural changes of methacryloyl groups, resulting in higher adhesive strength. The charge transfer interactions that play a major role in adhesion to zirconia are reflected in large DFT components in Fig. 6, which is a trend not observed in the adhesion of epoxy resins to engineering plastics, inorganic materials, and metallic materials analyzed in previous studies.[28–30,33,35,37] These results suggest that increasing the ratio of monoclinic surfaces may improve the adhesive strength of the interface. However, the methacryloyl group structure changes on the monoclinic surface, and this change may have a negative effect on the polymerization reaction in curing adhesive monomers such as 2-MEP. Moreover, monoclinic crystals are weaker in mechanical strength. Consequently, simply increasing the ratio of monoclinic crystals is insufficient, and an appropriate balance should be explored. These results promise to provide design guidelines for zirconia dental materials and adhesives.

4. Conclusions

To investigate the effects of zirconia crystal structure on the adhesion mechanism between zirconia dental materials and 2-MEP, clean and hydroxylated surfaces were constructed for
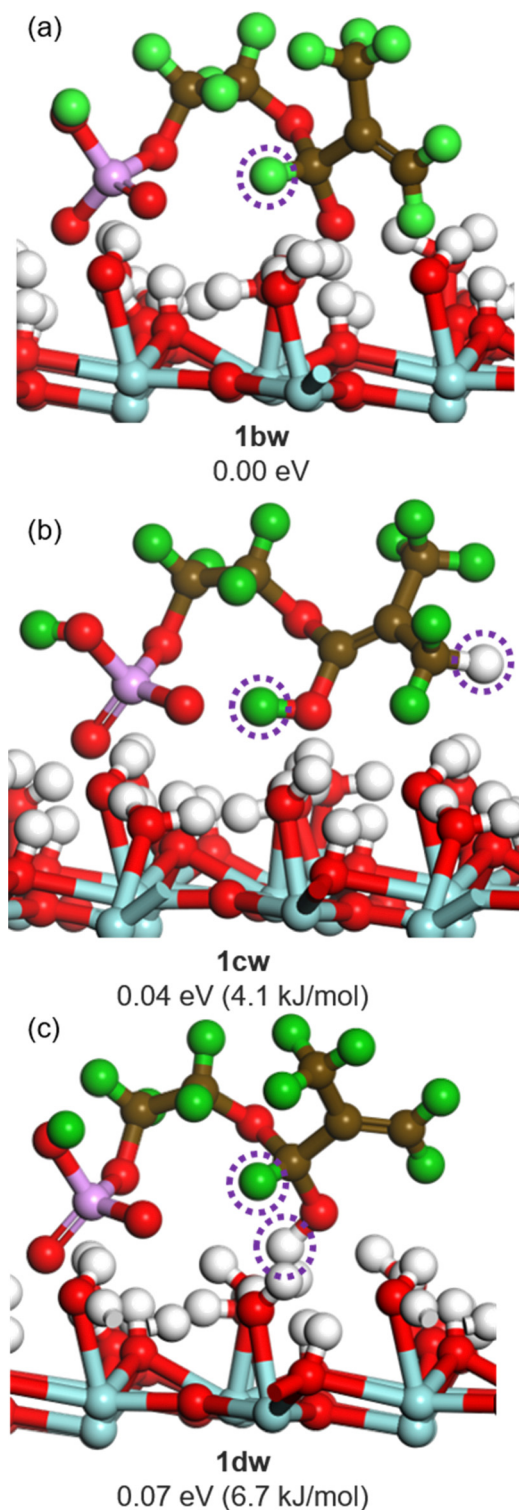
This journal is © The Royal Society of Chemistry 2025

J. Mater. Chem. B, 2025, **13**, 5095–5108 | **5105**

Fig. 12 Different structures of 2-MEP on the **1aw** surface. Energetically stable in order from (a)–(c).

at each adhesive interface, proton transfer from the phosphate group in 2-MEP occurred at all interfaces. Applying the charge density difference analysis, significant charge transfer interactions were observed on all surfaces, indicating that charge transfer interactions play an important role in adhesion. Applying the COHP analysis to these interfacial interactions, we found that the methacryloyl group in 2-MEP interacted particularly strongly with the m-ZrO$_2$ surfaces (**1b** and **1bw**). These interactions between the methacryloyl group and the surface were attributed to the low-coordination number of zirconium atoms on the m-ZrO$_2$ surface, which induced structural changes in the methacryloyl group. Concern must be raised in material design that the methacryloyl groups originally used for polymerization can undergo structural changes.

The above results provide a guideline for the design of zirconia dental materials and adhesives. The findings of this study could also contribute to the design of novel monomers for stronger adhesion and the optimization of zirconia surface treatments. In particular, new directions in the molecular design of adhesive monomers could be provided by considering the influence of the interaction of zirconium atoms with low coordination numbers on the m-ZrO$_2$ surface to the adhesive strength. Furthermore, the results of this study could contribute to the development of adhesive technology, not only for dental materials, but also for industrial applications and biocompatible materials. Further experimental validation based on the findings at the molecular level is required to advance the zirconia prosthetic materials and their clinical application.

Data availability

Data will be made available on request.

Conflicts of interest

There are no conflicts to declare.

Acknowledgements

References

1 C. Gross, T. Bergfeldt, T. Fretwurst, R. Rothweiler, K. Nelson and A. Stricker, *J. Mech. Behav. Biomed. Mater.*, 2020, **107**, 103759.
2 N. Cionca, D. Hashim and A. Mombelli, *Periodontol*, 2000, **73**, 241–258.

three different crystal surfaces m-ZrO$_2$, t-ZrO$_2$, and c-ZrO$_2$, and the adhesion mechanisms for these surfaces were discussed based on DFT calculations. The adhesive strengths for both clean and hydroxylated m-ZrO$_2$ surfaces are larger, which are attributed to the DFT component. Focusing on the interactions

3 R. C. Garvie, R. H. Hannink and R. T. Pascoe, *Nature*, 1975, **258**, 703–704.

4 M. Li, Z. Feng, G. Xiong, P. Ying, Q. Xin and C. Li, *J. Phys. Chem. B*, 2001, **105**, 8107–8111.

5 I. Denry and J. R. Kelly, *Dent. Mater.*, 2008, **24**, 299–307.

6 B. Stawarczyk, M. Özcan, L. Hallmann, A. Ender, A. Mehl and C. H. F. Hämmerlet, *Clin. Oral Invest.*, 2013, **17**, 269–274.

7 L. Mao, M. R. Kaizer, M. Zhao, B. Guo, Y. F. Song and Y. Zhang, *J. Dent. Res.*, 2018, **97**, 1222–1228.

8 M. N. Aboushelib, H. Mirmohamadi, J. P. Matinlinna, E. Kukk, H. F. Ounsi and Z. Salameh, *Dent. Mater.*, 2009, **25**, 989–993.

9 J. Y. Thompson, B. R. Stoner, J. R. Piascik and R. Smith, *Dent. Mater.*, 2011, **27**, 71–82.

10 M. Okada, K. Inoue, M. Irie, H. Taketa, Y. Torii and T. Matsumoto, *Dent. Mater. J.*, 2017, **36**, 600–605.

11 F. P. Nothdurft, P. J. Motter and P. R. Pospiech, *Clin. Oral Invest.*, 2009, **13**, 229–235.

12 M. Özcan and M. Bernasconi, *J. Adhes. Dent.*, 2015, **17**, 7–26.

13 E.-G. C. Tzanakakis, I. G. Tzoutzas and P. T. Koidis, *J. Prosthet. Dent.*, 2016, **115**, 9–19.

14 N. Nagaoka, K. Yoshihara, V. P. Feitosa, Y. Tamada, M. Irie, Y. Yoshida, B. V. Meerbeek and S. Hayakawa, *Sci. Rep.*, 2017, **7**, 45563.

15 Y. Chen, Z. Lu, M. Qian, H. Zhang, C. Chen, H. Xie and F. R. Tay, *Dent. Mater.*, 2017, **33**, e415–e427.

16 T. Kosmač, C. Oblak, P. Jevnikar, N. Funduk and L. Marion, *Dent. Mater.*, 1999, **15**, 426–433.

17 L. M. Schabbach, B. C. dos Santos, L. S. De Bortoli, D. Fabris, M. C. Fredel and B. Henriques, *Dent. Mater.*, 2023, **39**, 807–819.

18 X. Wang, J. Zhao, W. Sun, Y. Pei, J. An, Z. Li and J. Ren, *Comput. Mater. Sci.*, 2019, **159**, 210–221.

19 X. Wang, J. Zhao, Y. Li, S. Huang, J. An, R. Shi, Y. Pei, Z. Li and J. Ren, *Chem. Eng. Sci.*, 2021, **229**, 116018–116028.

20 X. Yang, L. Chen, X. Yu, J. Yu, D. Han, M. Xiao, M. Ge and X. Yang, *J. Mater. Chem. A*, 2023, **11**, 287–296.

21 Y. Morimitsu, H. Matsuno, Y. Oda, S. Yamamoto and K. Tanaka, *Sci. Adv.*, 2022, **8**, 6349.

22 S. Ogata and Y. Takahashi, *J. Phys. Chem. C*, 2016, **120**, 13630–13637.

23 G. Bahlakeh, M. Ghaffari, M. R. Saeb, B. Ramezanzadeh, F. De Proft and H. Terryn, *J. Phys. Chem. C*, 2016, **120**, 11014–11026.

24 K. Min, A. R. Rammohan, H. S. Lee, J. Shin, S. H. Lee, S. Goyal, H. Park, J. C. Mauro, R. Stewart, V. Botu, H. Kim and E. Cho, *Sci. Rep.*, 2017, **7**, 10475.

25 G. Bahlakeh and B. Ramezanzadeh, *ACS Appl. Mater. Interfaces*, 2017, **9**, 17536–17551.

26 S. Ogata and M. Uranagase, *J. Phys. Chem. C*, 2018, **122**, 17748–17755.

27 D. J. Eyckens, F. Stojcevski, A. Hendlmeier, J. D. Randall, D. J. Hayne, M. K. Stanfield, B. Newman, F. Vukovic, T. R. Walsh and L. C. Henderson, *J. Mater. Chem. A*, 2021, **9**, 26528–26572.

28 Y. Sumiya, Y. Tsuji and K. Yoshizawa, *Phys. Chem. Chem. Phys.*, 2022, **24**, 27289–27301.

29 Y. Sumiya, Y. Tsuji and K. Yoshizawa, *ACS Omega*, 2022, **7**, 17393–17400.

30 T. Uwabe, Y. Sumiya, Y. Tsuji, S. Nakamura and K. Yoshizawa, *Langmuir*, 2023, **39**, 18537–18547.

31 S. Chai, J. Liu, D. Hou and P. Wang, *RSC Adv.*, 2023, **13**, 30915–30924.

32 S. Ogata and M. Uranagase, *J. Phys. Chem. B*, 2023, **127**, 2629–2638.

33 A. Shrestha, Y. Sumiya, K. Okazawa, T. Uwabe and K. Yoshizawa, *Langmuir*, 2023, **39**, 5514–5526.

34 K. Hagita, T. Miyata and H. Jinnai, *Langmuir*, 2023, **39**, 7063–7078.

35 A. Shrestha, Y. Sumiya, K. Okazawa, Y. Tsuji and K. Yoshizawa, *Langmuir*, 2024, **40**, 21573–21586.

36 K. Kohei, Y. Sumiya, K. Okazawa, K. Yoshizawa, Y. Itoh and T. Aida, *J. Am. Chem. Soc.*, 2024, **146**, 21168–21175.

37 Y. Sumiya, R. Kaji and K. Yoshizawa, *Chem. Phys. Lett.*, 2024, **847**, 141370.

38 M. Nakatani, S. Fukamachi, P. Solis-Fernandez, S. Honda, K. Kawahara, Y. Tsuji, Y. Sumiya, M. Kuroki, K. Li, Q. Liu, Y.-C. Lin, A. Uchida, S. Oyama, H. G. Ji, K. Okada, K. Suenaga, Y. Kawano, K. Yoshizawa, A. Yasui and H. Ago, *Nat. Electron.*, 2024, **7**, 119–130.

39 C. J. Howard and R. J. Hill, *J. Mater. Sci.*, 1991, **26**, 127–134.

40 T. Aoyama, N. Kurata, K. Hirota and O. Yamaguchi, *J. Am. Ceram. Soc.*, 1995, **78**, 3163–3164.

41 D. J. Kim, S. H. Hyun, S. G. Kim and M. Yashima, *J. Am. Ceram. Soc.*, 1994, **77**, 597–599.

42 G. Kresse and J. Hafner, *Phys. Rev. B:Condens. Matter Mater. Phys.*, 1993, **47**, 558–561.

43 G. Kresse and J. Hafner, *Phys. Rev. B:Condens. Matter Mater. Phys.*, 1994, **49**, 14251–14269.

44 G. Kresse and J. Furthmüller, *Comput. Mater. Sci.*, 1996, **6**, 15–50.

45 J. P. Perdew and K. Burke, *Phys. Rev. Lett.*, 1996, **77**, 3865–3868.

46 S. Grimme, *J. Comput. Chem.*, 2006, **27**, 1787–1799.

47 G. Kresse and D. Joubert, *Phys. Rev. B: Condens. Matter Mater. Phys.*, 1999, **59**, 1758–1775.

48 B. Adolph, J. Furthmüller and F. Beckstedt, *Phys. Rev. B: Condens. Matter Mater. Phys.*, 2001, **63**, 125108.

49 S. T. Korhonen, M. Calatayud and A. O. I. Krause, *J. Phys. Chem. C*, 2008, **112**, 6469–6476.

50 W. Piskoz, J. Grybos, F. Zasada, S. Cristol, J. F. Paul and Z. Sojka, *J. Phys. Chem. C*, 2011, **115**, 24274–24286.

51 A. Hofman, S. J. Clark, M. Oppel and I. Hahndorf, *Phys. Chem. Chem. Phys.*, 2002, **4**, 3500–3508.

52 R. Anez, A. Sierralta and P. Sautet, *J. Phys. Chem. C*, 2007, **111**, 8314–8320.

53 J. Yang, J. Ren, H. Guo, X. Qin, B. Han, J. Lin and Z. Li, *RSC Adv.*, 2015, **5**, 59935–59945.

54 H. Y. T. Chen, S. Tosoni and G. Pacchioni, *Surf. Sci.*, 2016, **652**, 163–171.

This journal is © The Royal Society of Chemistry 2025

J. Mater. Chem. B, 2025, **13**, 5095–5108 | 5107

55 K. Momma and F. Izumi, *J. Appl. Crystallogr.*, 2011, **44**, 1272–1276.

56 BIOVIA Materials Studio. Materials studio 2020; Dassault Systèmes: San Diego, 2020.

57 B. Leimkuhler, E. Noorizadeh and F. A. Theil, *J. Stat. Phys.*, 2009, **135**, 261–277.

58 H. Sun and P. Ren, *Comput. Theor. Polym. Sci.*, 1998, **8**, 229.

59 A. Abbasi, *RSC Adv.*, 2019, **9**, 16069–16082.

60 S. Steinberg and R. Dronskowski, *Crystals*, 2018, **8**, 225.

61 S. Maintz, V. L. Deringer, A. L. Tchougréeff and R. Dronskowski, *J. Comput. Chem.*, 2016, **37**, 1030–1035.

62 R. Dronskowski and P. E. Blöchl, *J. Phys. Chem.*, 1993, **97**, 8617–8624.

63 V. L. Deringer, A. L. Tchougréeff and R. Dronskowski, *J. Phys. Chem. A*, 2011, **115**, 5461–5466.

5108 | *J. Mater. Chem. B*, 2025, **13**, 5095–5108

This journal is © The Royal Society of Chemistry 2025